Electronic Supplementary Information

High Photoluminescence Quantum Yield Near-Infrared Emission from a Lead-Free Ytterbium-Doped Double Perovskite

*Minh N. Tran, Iver J. Cleveland, Joseph R. Geniesse, and Eray S. Aydil**

Department of Chemical and Biomolecular Engineering, Tandon School of Engineering, New York University, Brooklyn, New York 11201, USA

Corresponding Author

*Email: aydil@nyu.edu

Table of Contents

1. Calculation of the minimum near-infrared photoluminescence quantum yield needed to increase the efficiency of a solar cell with a given external quantum efficiency

Consider a solar cell with power conversion efficiency, η, external quantum efficiency, $EQE(\lambda)$, open-circuit voltage, V_{OC} and fill factor FF. When this solar cell is coated with a material that downconverts UV-blue photons to NIR photons, the downconversion (DC) material absorbs in the UV-blue region of the electromagnetic spectrum and reemits in the near-infrared (NIR) region. The new downconverted photon flux the solar cell receives is

$$\phi^*(\lambda) = \phi(\lambda) - A(\lambda) + \eta_{PLQY}\, f(\lambda) \int_0^{\lambda_{g,p}} A(\lambda)\, d\lambda \tag{1}$$

where $\phi(\lambda)$ is the unconverted solar photon flux (*e.g.,* AM1.5), λ is the wavelength (nm), $A(\lambda)$ is the film's absorbance, η_{PLQY} is the NIR photoluminescence quantum yield, and $f(\lambda)$ is the line shape of the NIR emission modeled as a Gaussian function

$$f(\lambda) = a e^{\frac{(x-b)^2}{c^2}} \tag{2}$$

where a, b and c (a= 3.84, b= 1004 nm, c= 26.08 nm^2)) are parameters determined by fitting a typical experimental NIR emission spectrum. For $Cs_2AgBiBr_6$, the wavelength corresponding to the perovskite bandgap, $\lambda_{g,p}$, is 560 nm. However, λ_{eg} is chosen to be 470 nm because of negligible absorbance and scattering interference at a wavelength higher than 470 nm. The short circuit current created from this downconverted photon flux is given by

$$J_{sc}^* = e \int_0^{\lambda_{g,Si}} \phi^*(\lambda)\, EQE(\lambda)\, d\lambda \tag{3}$$

where e is the electron charge and $EQE(\lambda)$ is the solar cell's external quantum efficiency. In our calculations, we digitized and used the $EQE(\lambda)$ data from references 1 and 2, for CIGS and Si, respectively. We assume that the open-circuit voltage and fill factor, V_{OC} and *FF,* remain the same and use the values from the same reference. The new power conversion efficiency of the solar cell receiving the downconverted solar spectrum is

$$\eta^* = J_{sc}^* \times V_{OC} \times FF. \tag{4}$$

Using these equations, we can back-calculate the minimum η_{PLQY} required for η^* to exceed the original efficiency of the solar cell without the downconverting coating. For the solar cells and V_{OC}, FF and $EQE(\lambda)$ values from references 1 and 2, we obtain 67% and 69% for typical CIGS and Si solar cells, respectively.

2. Experimental details: Thin-film deposition

Films were deposited in a glove-boxed physical vapor deposition (PVD) system (Angstrom Engineering) with six evaporation sources. The four precursors, $BiBr_3$ (99%, Alfa Aesar), AgBr (99.9%, Beantown Chemical), CsBr (99.9%, Acros Organics), and $YbBr_3$ (hydrate, 99.99%, Alfa Aesar), were loaded into separate RADAK sources and baked overnight at 60, 100, 100, and 110 ºC, respectively. $BiBr_3$ was loaded in quartz ampoules, while the others were loaded in alumina ampoules. The glass substrates (25×25 mm^2) were cleaned by sonicating in a 1:1 solution by volume of acetone (ACS Grade, VWR) and isopropanol (99.5%, VWR) for 30 minutes, dried in an oven, and cleaned with O_2 plasma for 30 minutes using Expanded Plasma Cleaner PDC-001-HP (Harrick Plasma) before loading them onto the substrate holder. Each precursor's evaporation rate was monitored during the deposition by separate quartz crystal microbalances (QCMs). The substrates' temperatures were not controlled during the deposition. The tooling factors were determined by evaporating CsBr and $BiBr_3$ separately and obtaining the film thickness from interference fringes in optical transmission. The tooling factors, the ratio of the deposition rate at the substrate to the deposition rate at the QCM expressed as %, were 39.7 and 42.9 for CsBr and $BiBr_3$, respectively. The tooling factor of CsBr was also used for $YbBr_3$ and AgBr.

During the deposition of $Cs_2AgBiBr_6$ films, $BiBr_3$, AgBr, and CsBr were co-evaporated onto glass substrates at 1.00, 0.37, and 1.21 Å/s, respectively. With these deposition rates, CsBr to BiBr3 to AgBr molar flux ratio is 2:1:1. The CsBr, $BiBr_3$, and AgBr source temperatures were the manipulated variables to keep the evaporation rates constant and were ≈555, 140, and 650 ºC, respectively. The controller adjusts the temperature around these values to keep the deposition rate constant at the setpoints.

For Yb-doped $Cs_2AgBiBr_6$ films, three precursors, $BiBr_3$, AgBr, and $YbBr_3$, were co-deposited on glass substrates. CsBr was deposited on top of this $BiBr_3$-AgBr-$YbBr_3$ layer. $BiBr_3$ and AgBr evaporation rates were kept constant at 1.00 Å/s and 0.37 Å/s, respectively, while the $YbBr_3$ evaporation rate varied from 0.03 to 0.14 Å/s to change the amount of Yb doping. The $YbBr_3$ source temperature ranged from 627 to 688 ºC, depending on the evaporation rate and precursor amount in the ampoule. The CsBr evaporation rate was 1.21 Å/s. The system base pressure was 6×10^{-7} Torr, while the chamber pressure rose to $\approx10^{-6}$ Torr during the deposition. Each layer was deposited for 30 minutes, resulting in 490±10 nm thick films for $Cs_2AgBiBr_6$. The optical absorption spectrum was obtained from thinner films deposited for 15 minutes to avoid saturation. Films were annealed on a hot plate in the glovebox at different temperatures and durations (See main text).

For $Cs_2AgBiCl_{6-y}Br_y$ thin films, chloride salts were used along with bromide salts to achieve the target halide ratio: $Cs_2AgBiClBr_5$ films were deposited using AgCl, $BiBr_3$ and CsBr; $Cs_2AgBiCl_3Br_3$ films were deposited using AgCl, $BiBr_3$ and CsCl; $Cs_2AgBiCl_4$ Br_2 films were deposited using AgCl, $BiCl_3$ and CsBr. The evaporation rates of AgCl, $BiBr_3$, $BiCl_3$, CsBr and CsCl were 0.33, 1.00, 0.85, 1.21 and 1.07 Å/s, respectively. Precursors were co-evaporated onto glass substrates for 30 minutes, and the films were then annealed at 300 ºC for one hour.

3. Experimental details: Thin-film characterization

All films were characterized under ambient conditions at room temperature. Photoluminescence (PL) spectra were measured using a QuantaMaster-8075-21 (Horiba) spectrophotometer. Visible PL from all films was excited at 420 nm (5 nm bandwidth) with double monochromator filtered emission from a Xe-arc lamp and detected using a PMT detector. Near-infrared PL was excited at 420 nm for all films. For the film with the highest PLQY (8% Yb-$Cs_2AgBiBr_6$), the excitation wavelength was varied between 360 to 600 nm to examine the PLQY dependence on the excitation wavelength. NIR PL was detected using a liquid nitrogen-cooled InGaAs detector. PLQY was measured using an integrating sphere (Quanta-Phi, Horiba), and the lamp power was measured using Power Meter 843-R and 818-UV photodetector (Newport). Details of PLQY measurements are published in our previous work.[3] X-ray diffraction (XRD) patterns from the films were recorded using a Bruker D8 Discover General Area Detector Diffraction System (GADDS) equipped with a Cu-Kα source. Raman spectra were acquired using a Thermo Scientific DXR Raman microscope. Thin films were excited with a 785 nm laser, and Raman scattering in the range of 50-1800 cm^{-1} was collected with a 50× Olympus objective, dispersed using a high resolution (2 cm^{-1}) grating, and detected with a CCD detector. Films were examined using a Merlin field emission scanning electron microscope (Carl Zeiss, 5 kV, 110 pA). Their average composition over approximately 10 μm^2 was determined using energy-dispersive X-ray spectroscopy (Oxford Instruments EDS) and vendor-provided sensitivity factors. Optical absorptions of the films were recorded using an Agilent Cary 5000 UV-Vis-NIR in the 200-2000 nm range.

4. Bohr radius calculation

Exciton Bohr radius is given by

$$a_{ex} = \varepsilon_r \frac{m_o}{\mu_r} a_B \tag{5}$$

where ε_r is the dielectric constant ($\varepsilon_r \sim 5.8$),[4] m_o is the mass of an electron, a_B=0.053 nm is the Hydrogen Bohr Radius and μ_r is the reduced mass given by

$$\mu_r = \frac{m_e m_h}{m_e + m_h} \tag{6}$$

Taking $m_e = 0.37m_o$ and $m_h = 0.14m_o$ from reference 5, we obtain $a_{ex} \approx 0.03$ nm. Taking $m_e = 0.36m_o$ and $m_h = 0.33\, m_o$ from reference 6, we obtain $a_{ex} \approx 0.05$ nm. Both these estimates are much smaller than the unit cell dimensions.

5. XRD and Raman spectra from as-deposited films showing the unreacted and impurity phases

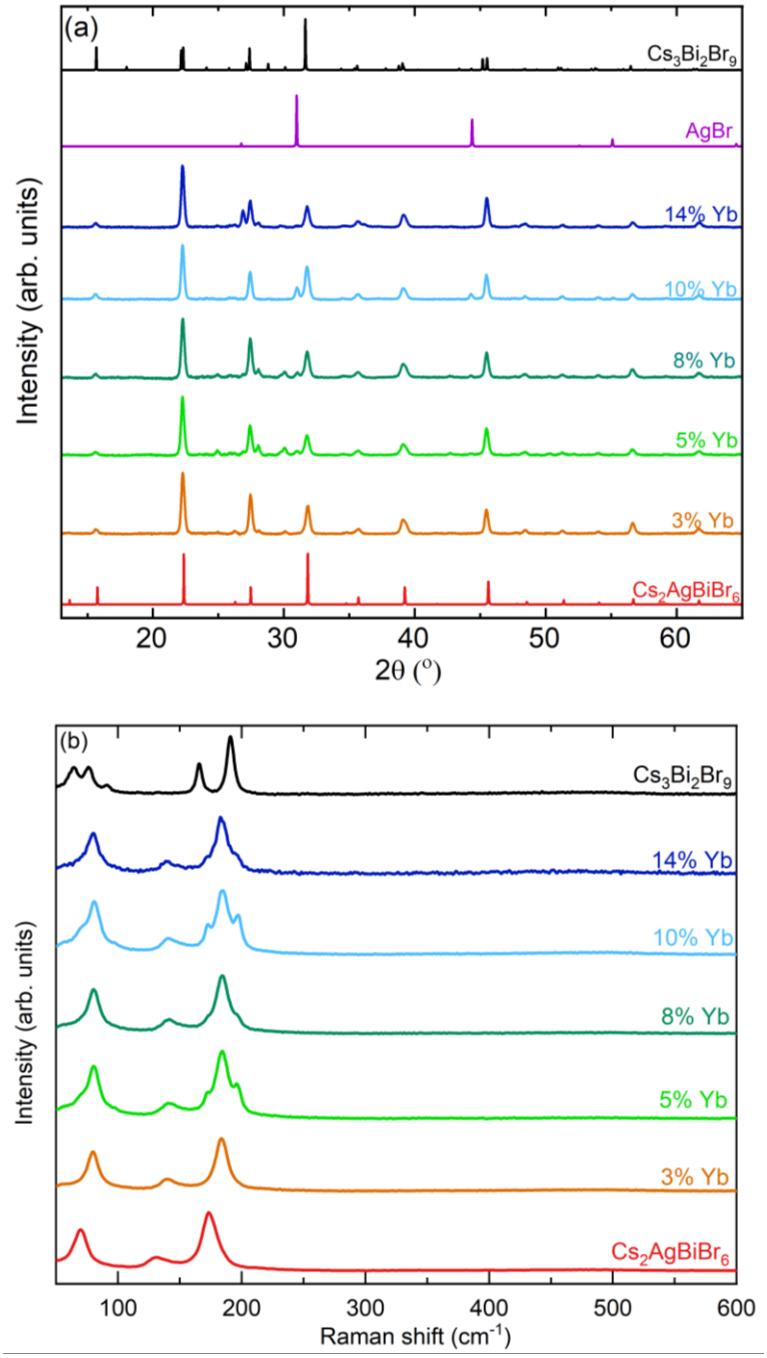

Fig. S1. (a) X-ray diffraction patterns and (b) Raman spectra of as-deposited Yb-doped $Cs_2AgBiBr_6$ films. XRD of films doped with 5-14% Yb show multiple weak peaks that do not belong to $Cs_2AgBiBr_6$. Films doped with 5-14% Yb have Raman peaks at 197 and 170 cm^{-1}, which belong to an impurity phase, $Cs_3Bi_2Br_9$. Some impurity phase peaks match with the XRD of AgBr and $Cs_3Bi_2Br_9$. Simulated (using VESTA software[7]) XRD patterns of AgBr, $Cs_2AgBiBr_6$, and $Cs_3Bi_2Br_9$ using CIF files from references 8, 9, and 10, respectively, are shown for comparison.

6. Lattice Parameters of undoped and Yb doped $Cs_2AgBiBr_6$

Table S1. Lattice parameters (a) of undoped and Yb-doped $Cs_2AgBiBr_6$ films from XRD data. The lattice parameters are averaged of three values calculated from the following (hkl): (220), (400), and (222).

% Yb	a (Å)
0	11.282
3	11.252
5	11.278
8	11.270
10	11.272
14	11.296

7. SEMS of Yb-doped films annealed under different conditions

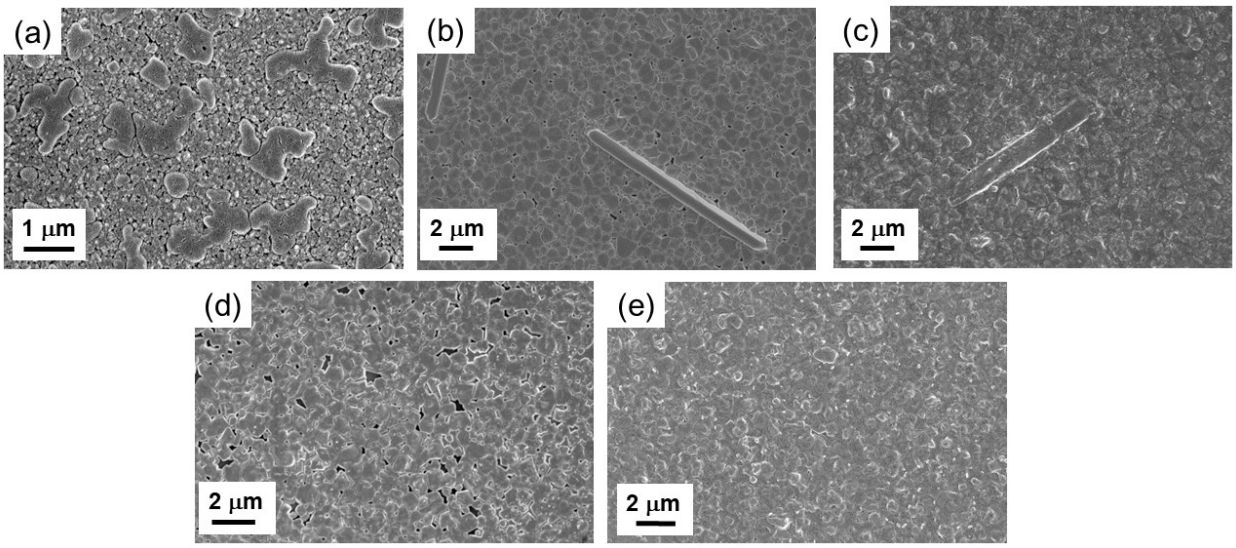

Fig. S2. Scanning electron micrographs (SEMs) of Yb-doped (10% Yb) $Cs_2AgBiBr_6$ films annealed in a nitrogen-filled glove box under different conditions showing the effects of annealing temperature and annealing duration. In the top row, from left to right, are SEMs of (a) as-deposited films, (b) films annealed at 250 ºC for 1 hour, and (c) films annealed at 250 ºC for 2 hours. At the bottom row, from left to right, are SEMs of (d) films annealed at 300 ºC for 1 hour and (e) films annealed a 300 ºC for 2 hours. The average composition of the larger crystal domains (*e.g.,* large irregular domains in (a) and elongated crystals in (b) and (c) is 57.2% Br, 16.9% Ag, 21.4% Cs, 0.3% Yb, and 4.2% Bi, suggesting that the impurity is a Cs-Ag-Br phase, possibly $CsAgBr_2$ (#63, Cmcm). The small Bi signal detected is likely coming from the $Cs_2AgBiBr_6$ surrounding or beneath these regions.

8. Effect of the annealing temperature and duration on the Raman Spectra, XRD, and SEMs of undoped $Cs_2AgBiBr_6$ films

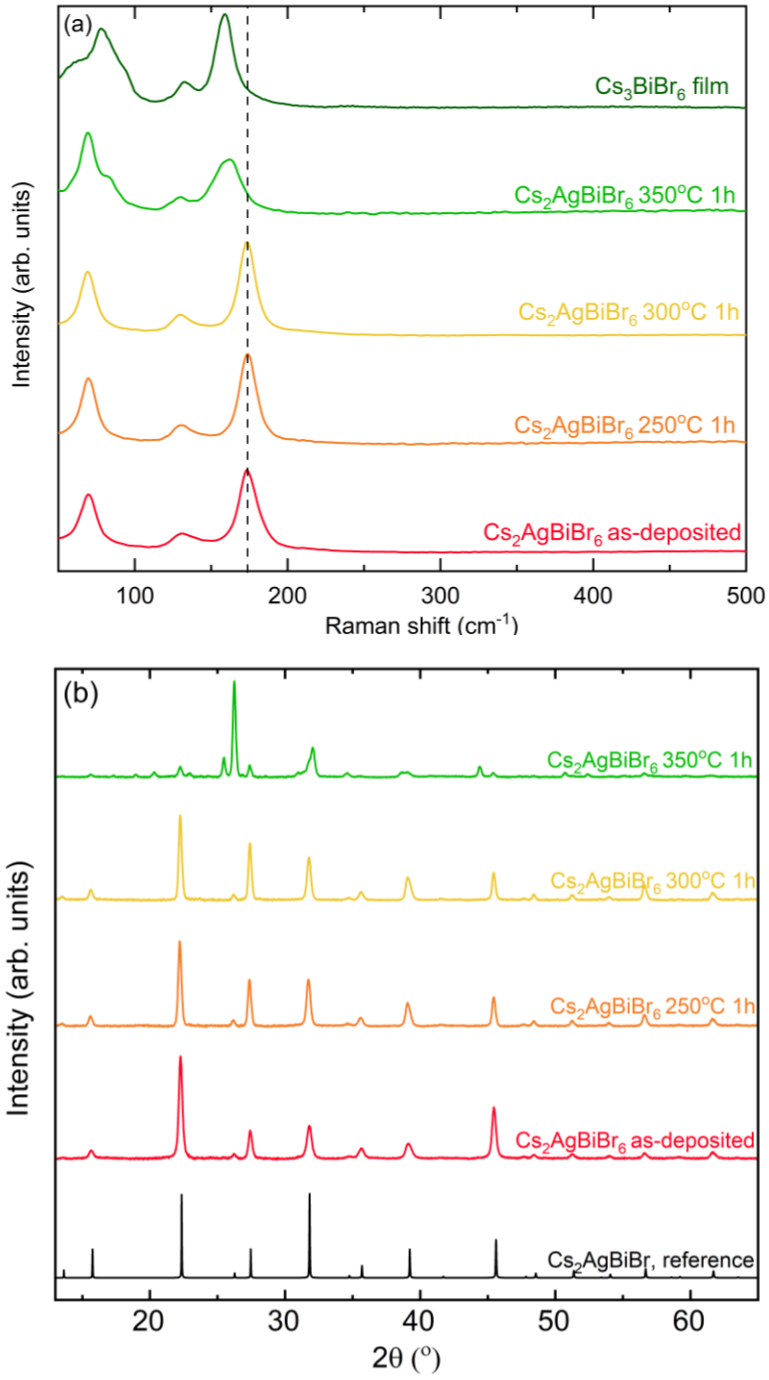

Fig. S3. (a) Raman scattering and (b) XRD from $Cs_2AgBiBr_6$ as-deposited films and films annealed at different temperatures. When annealed at 350 °C, $Cs_2AgBiBr_6$ decomposes, possibly to Cs_3BiBr_6, as shown in the Raman spectra.

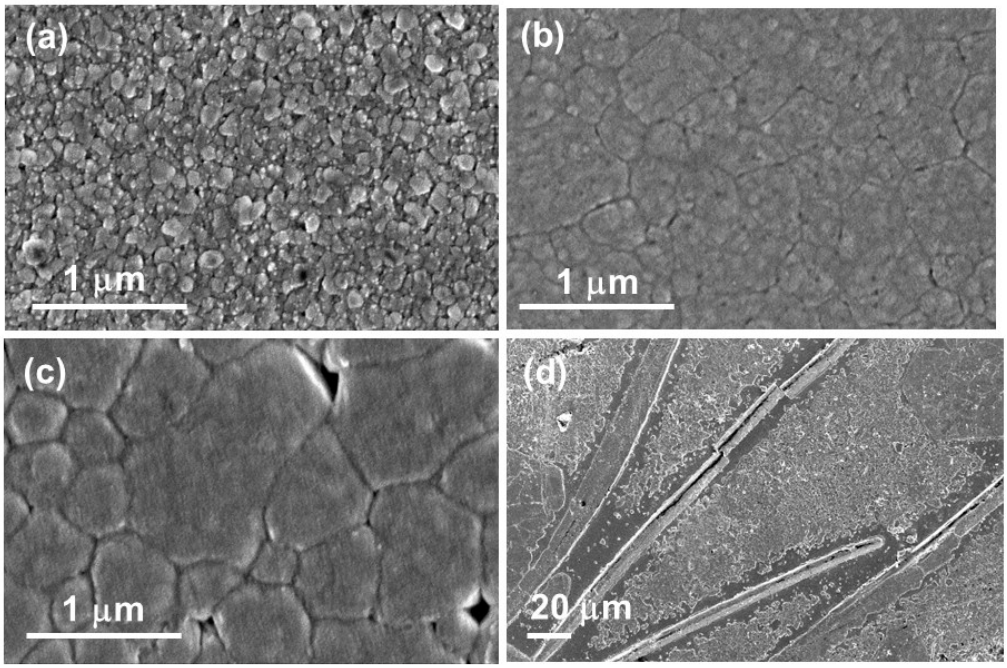

Fig. S4. SEM images of $Cs_2AgBiBr_6$ films annealed at different temperatures for 1 hour: (a) as-deposited, (b) 250 ºC; (c) 300 ºC, and (d) 350 ºC. Films decompose when annealed at 350 ºC.

9. Effect of Yb doping level on the microstructure of $Cs_2AgBiBr_6$ films annealed under optimized annealing conditions

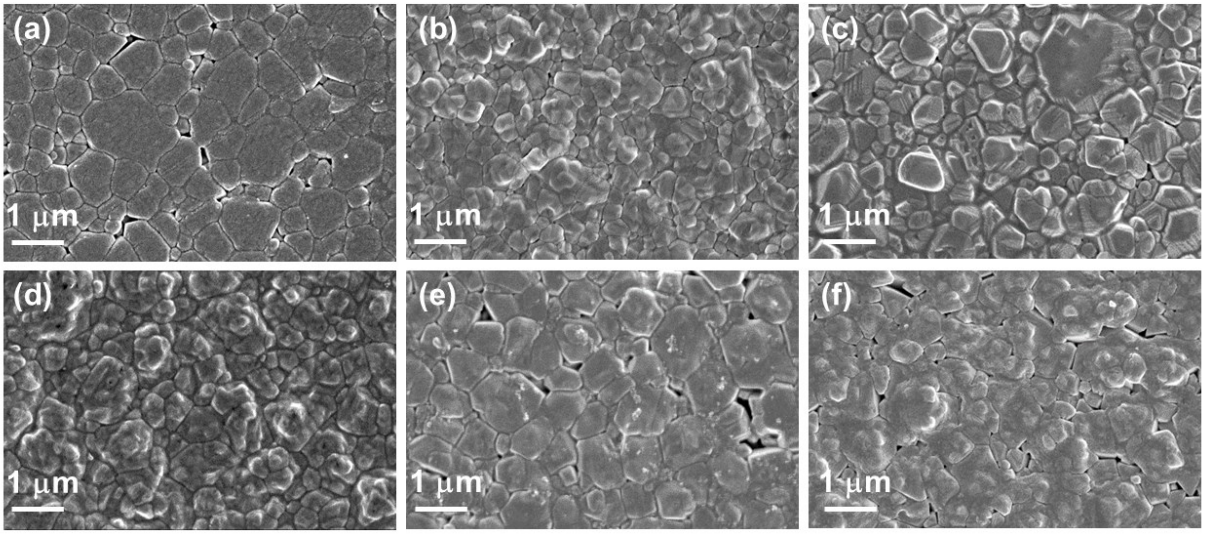

Fig. S5. SEM images of $Cs_2AgBiBr_6$ films doped with 0-14% Yb annealed at 300 ºC for 1 hour: (a) 0% Yb, (b) 3% Yb, (c) 5% Yb, (d) 8% Yb, (e) 10% Yb, and (f) 14% Yb.

10. XRD patterns from $Cs_2AgBiCl_yBr_{6-y}$ thin films

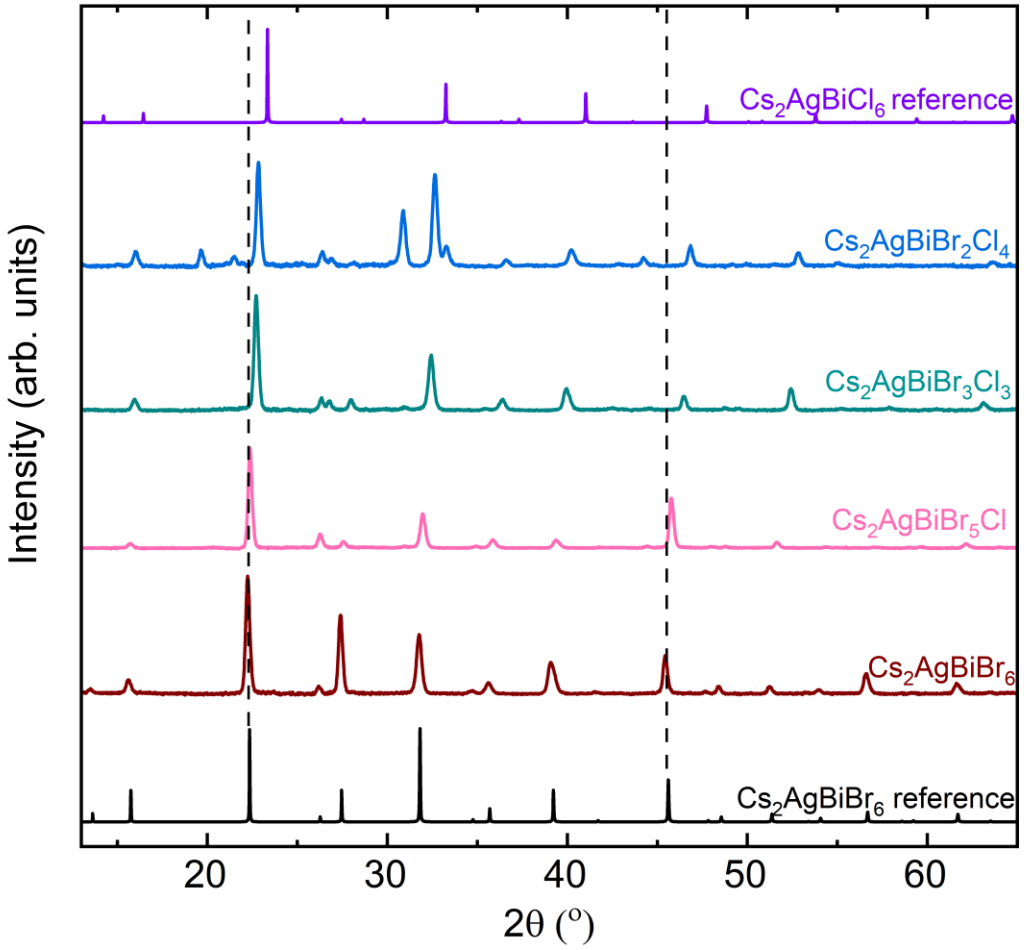

Fig. S6. XRD patterns from $Cs_2AgBiCl_yBr_{6-y}$ thin films, and simulated XRD patterns of $Cs_2AgBiCl_6$ and $Cs_2AgBiBr_6$. As dotted lines show, XRD peaks are shifted to higher 2θ values with increasing amounts of chlorine, suggesting that two halide ions are mixed throughout the films. XRD $Cs_2AgBiBr_2Cl_4$ contains impurity peaks of $Cs_2AgBiCl_6$, suggesting phase segregation in this film after annealing.

11. Annealing Dependence of the Orange Photoluminescence

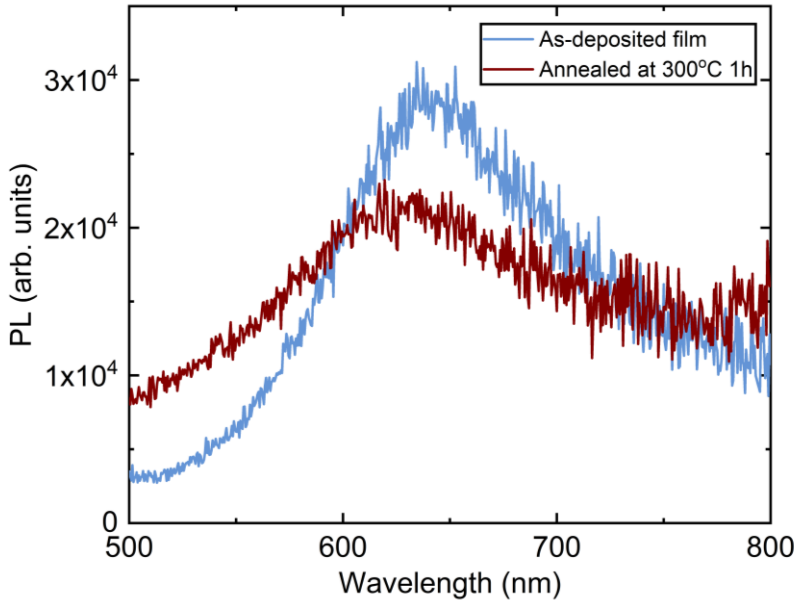

Fig. S7. Orange photoluminescence from $Cs_2AgBiBr_6$ thin film decreases after annealing at 300 °C for one hour.

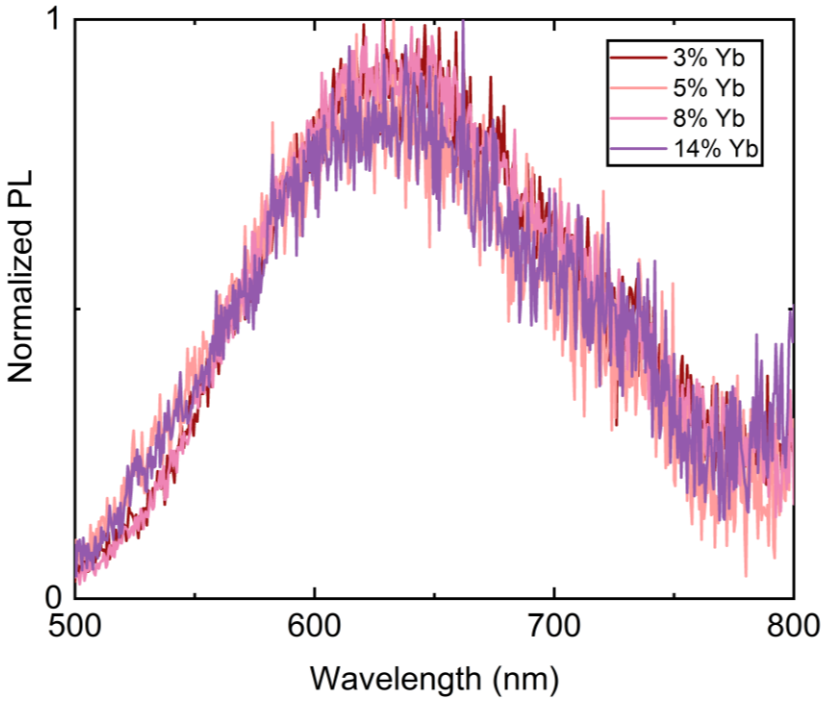

Fig. S8. Orange emission from $Cs_2AgBiBr_6$ thin films doped with 3-14% Yb. Emissions at all Yb levels are weak, as the noise suggests. However, the orange emission from 10% Yb-$Cs_2AgBiBr_6$ film was particularly weak, and it is difficult to distinguish between the film's PL and stray light, so its PL is not included here.

12. Air stability of the PLQY

Table S2. NIR PLQY of $Cs_2AgBiBr_6$ films doped with 3% Yb on the day of the deposition and after one day in the air. The excitation wavelength was 420 nm with 10 nm bandwidth. Dependence of one-day stability of PLQY is shown for different annealing times and temperatures.

Annealing Temperature	Annealing Time	PLQY after Annealing	PLQY after one day
300 ºC	1 hour	75.1%	78.3%
300 ºC	2 hours	72.1%	74.3%
250 ºC	1 hour	67.1%	50.1%
250 ºC	2 hours	66.4%	54.1%

13. Yb concentration dependence of NIR PLQY

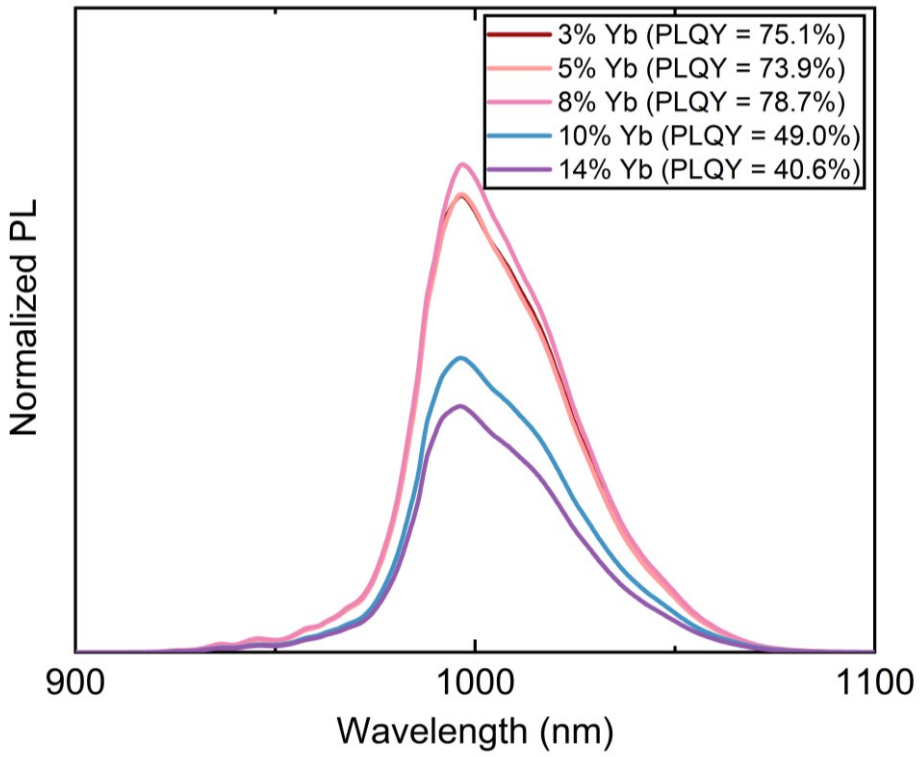

Fig. S9. PLQY of $Cs_2AgBiBr_6$ films doped with 3 to 14% Yb and annealed at 300 ºC for one hour. Normalized PL means the PL intensity of each film is scaled with PLQY.

14. Calculation of Si and CIGS solar cell efficiencies with a downconverting overlayer

Using the $EQE(\lambda)$ from references 1 and 2 for typical CIGS and Si solar cells, respectively, we calculated the efficiency increase when these solar cells are coated with a downconverting overlayer with a PLQY of 82.5%. We conservatively assume that the open-circuit voltage and fill factor, V_{OC} and *FF,* remain the same and use the values from the same references. Figure S10 shows the photocurrent action spectrum at short circuit with $[J_{sc}^{*}\ (\lambda)]$ and without $[J_{sc}\ (\lambda)]$ a downconversion overlayer. The new power conversion efficiency of the solar cell receiving the downconverted solar spectrum is

$$\eta^{*} = J_{sc}^{*} \times V_{OC} \times FF \tag{4}$$

where J_{sc}^{*} is the integrated photocurrent action spectrum at short circuit.

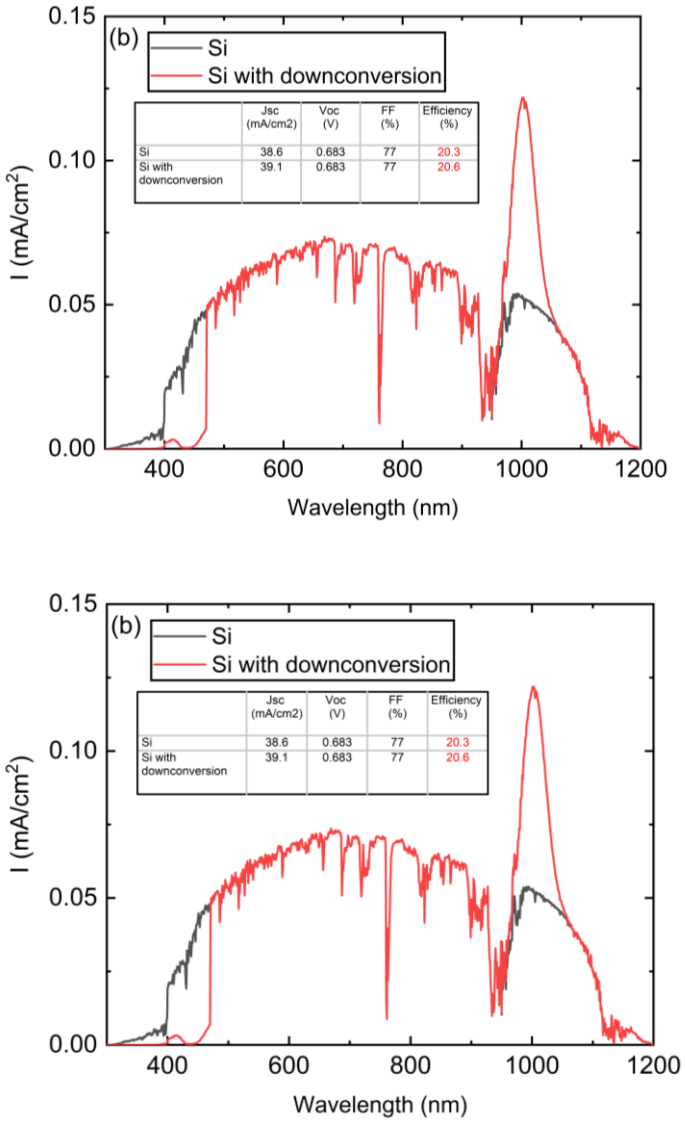

Fig. S10. The photocurrent action spectrum of a typical (a) CIGS[1] and (b) Si solar cell[2] changes after a layer of down-conversion materials is deposited on top of a solar cell. For example, with 82.5% of PLQY, the solar cell's efficiency can increase from 20.4 to 20.7% for CIGS and 20.3 to 20.6% for Si.

References

1. T. M. Friedlmeier, P. Jackson, A. Bauer, D. Hariskos, O. Kiowski, R. Wuerz and M. Powalla, *IEEE 42nd Photovoltaic Specialist Conference*, 2015, 1-3.
2. L. Mazzarella, S. Kirner, B. Stannowski, L. Korte, B. Rech and R. Schlatmann, *Appl. Phys. Lett*., 2015, **106**, 023902.
3. M. N. Tran, I. J. Cleveland, G. A. Pustorino and E. S. Aydil, *J. Mater. Chem. A*, 2021, **9**, 13026–13035.
4. M. R. Filip, S. Hillman, A. A. Haghighirad, H. J. Snaith and F. Giustino, *J. Phys. Chem. Lett*., 2016, **7**, 2579−2585.
5. E. T. McClure, M. R. Ball, W. Windl and P. M. Woodward, *Chem. Mater.,* 2016, **28**, 1348−1354.
6. G. Volonakis, M. R. Filip, A. A. Haghighirad, N. Sakai, B. Wenger, H. J. Snaith and F. Giustino, *J. Phys. Chem. Lett*. 2016, **7**, 1254−1259.
7. K. Momma and F. Izumi, *J. Appl. Crystallogr*., 2011, **44**, 1272-1276.
8. R. W. G. Wyckoff, Crystal Structures, Second edition. *Interscience Publishers, New York, New York*. 1963, **1**, 7-83.
9. A. H. Slavney, T. Hu, A. M. Lindenberg and H. I. Karunadasa, J. *Am. Chem. Soc*., 2016, **138**, 2138−2141.
10. F. Lazarini, *Acta Cryst*., 1977, **B33**, 2961-2964.